Improving predictability of additively manufactured Ti-6Al-4 V lattices for orthopaedic devices: A parametric and struts angle study

Xue Cao [a], Luke N. Carter [a], Kenny Man [a,b], Victor M. Villapún [a], Lucie Giangiorgi [a,c], Sophie C. Cox [a,*]

[a] School of Chemical Engineering, College of Engineering and Physical Sciences, University of Birmingham, Edgbaston B15 2TT, UK
[b] Department of Oral and Maxillofacial Surgery & Special Dental Care, University Medical Centre Utrecht, PO 85500, Utrecht GA 3508, The Netherlands
[c] Department of Biomedical Engineering, Polytech & Aix-Marseille Université, Marseille 13009, France

ARTICLE INFO

ABSTRACT

The advancement of metal additive manufacturing has recently enabled the integration of porous lattice regions into orthopaedic devices. Despite the increased utilisation of various metamaterials there remains limited understanding of how to optimise laser process specifically for these geometries. Selective laser melting (SLM) of representative single struts is focused on this study from the perspective of surface properties, mechanical performance, and in-vitro biological response. Specifically, the influence of laser power (100 – 200 W) and speed (2250 – 900 mm/s) and struts angle (20–90°) for a 250μ m strut diameter was explored. Struts built below 45° to the substrate using optimal laser parameters (150 W and 1125 mm/s) were found to exhibit a surface topography that facilitated the highest level of cell adhesion (84.3 cells/mm^2) after 24 hrs (p $\leq$ 0.001). To support this finding, a novel image analysis method was developed to characterise the average roughness across the complete strut profile. An opposite trend was observed for mechanical strength with struts built at above 45° without failure. These findings were brought together in a parameter design map was to guide stakeholders in producing customised biomedical devices, enabling control of key physiochemical properties with the aim of maximising osseointegration.

1. Introduction

The global orthopaedic devices market is predicted to reach USD 73 billion by 2032, due to an ageing population and an increasing number of traumatic injuries as well as bone disorders [1,2]. Ti-6Al-4 V (Ti64) has been a widely used biomaterial for bone implants benefitting from its biocompatibility, mechanical properties, and corrosion resistance [3]. However, compared to natural bone, the inherent high strength and stiffness of solid metal components shields the stress that stimulates bone cell growth, resulting in an unbalanced load distribution between native bone and implanted device. Known as stress shielding, it increases the risk of revision surgery due to aseptic loosening [4], although it has been shown that controlled and customised metal scaffolds can minimise this effect [5]. Open cellular lattice structures as *meta*-biomaterials, consisting of regular or stochastically connected struts and nodes, are designed to reduce the bulk stiffness of the material, as well as providing a larger surface-to-volume ratio to enhance osseointegration [6]. Control of geometric lattice parameters, such as unit cell type, strut thickness, designed pore size, etc., have been shown to provide specific functional characteristics [7–11].

In addition to facilitating osseointegration, a number of other advantages of porous lattices have been proposed, including their use as reservoirs to release therapeutic agents without losing mechanical strength, bone-mimetic platforms to enhance pro-regenerative extracellular vesicle production or as strategic features capable to mitigate magnetic resonance imaging (MRI) artefacts, further increasing their potential in regenerative medicine [12–14]. However, the complexity of lattices makes them difficult to be manufactured by conventional substrative processes. In this regard, Additive Manufacturing (AM) techniques and, more specifically, Selective Laser Melting (SLM), offers unsurpassed freedom to produce these beneficial porous structures [15]. SLM manufacturing flexibility is enabled by the layer-by-layer conformation of three dimensional parts through selectively melting and solidifying feedstock powder according to a computer-aided design (CAD) guided design [16]. Despite the advantages of SLM, process issues including partially melted particles attached to the surface, selection of

---

* Corresponding author.
E-mail address: s.c.cox@bham.ac.uk (S.C. Cox).

in-process parameters, and the inherent rapid and localised heating and cooling could limit lattices prospective use of ideal surface finish and controlling of mechanical strength for biomedical devices [17]. Thus, the predictability, consistency, and manufacturability of AM implantable lattices need to be further explored.

It has been reported that the selection of SLM process parameters affects the final quality of lattices. This is especially important for lattices used in medical devices where geometric accuracy and surface finish directly influence performance [17]. Varying key process parameters, namely, laser power and scanning speed, has been found to influence formation of defects within lattices, including keyhole and gas porosity, lack of fusion defects, and balling behaviour [18]. Process parameters were also shown to strongly influence surface quality of SLMed components, particularly in down-facing regions, where greater energy input drove formation of a larger melt pool resulting in a poorer surface due to increased particle adhesion, entrapment, and sintering [19]. Likewise, inappropriate process parameters impact manufacturing accuracy, leading to oversized/undersized and irregular struts [20]. These geometric inaccuracies have been shown to negatively influence mechanical performance including deformation behaviour and failure mode [21]. Wang et al. found that scan speed plays a key role in the transformation of grain shape of Ti64 microstructure due to altered thermal history [22], while Ahmadi et al. concluded that the effect of process parameters is not significant to the grain size and shape of Ti64 lattices [23]. Collectively, properties such as surface finish and manufacturing accuracy varied with process parameters together bring challenges to the predictability of lattice production.

Alongside process parameters, the effect of struts angle on surface finish and manufacturing defects (internal pores), which influences mechanical performance, have been reported [24]. Changing deformation and failure behaviour between lattices consisted of different struts angles were observed by Mazur et al., with failure occurring mostly in struts built in the diagonal and vertical angle, with bending and buckling behaviour in lattices [25]. Both Murchio et al. and Hossain et al. studied the struts angle effect on tensile properties, the former concluded that build angle of struts has no obvious regularity on tensile properties, the latter found that there is an increasing trend of ultimate tensile strength as a function of struts angle [24,26]. These suggest that the importance to analyse, calculate, and control the local stress and strain of lattices. There has also been work demonstrating that the differences in surface topography of surfaces built at different angles may significantly alter osteoblast and bacterial attachment [27]. In summary, limited work brings together the influence of both process parameters and build angle on key success criteria for utilisation in medical devices, including surface quality, mechanical performance, and biological response. With this in mind, our objective is to understand the effect of process parameters and struts angle on fundamental properties of lattice element that drive these performance criteria. While it may be challenging to balances these criteria for orthopaedic device performance ultimately moving in this direction will improve predictability and quality.

Herein, a robust assessment to the effects of SLM process parameters and struts angle on surface roughness, three-point bending properties, and mammalian cell response has been conducted. To enable these fundamental relationships to be broadly utilised by the field a map to guide the design of lattices for tissue regeneration has been developed. Overall, this work initiates from fundamental study aiming to innovatively enable control, prediction, and improvement of implantable lattice fabrication within customised biomedical devices applied in bone replacement, maxillofacial, craniofacial, dental implants etc.

2. Materials and methods

2.1. Specimen manufacturing

A strut diameter of 250μ m was selected as being representative of lattices used in orthopaedic devices and used throughout this study [28].

10 mm long single struts at build angles of 20°, 45°, 70° and 90° to the substrate plate were designed in nTopology (version 3.35.2, nTopology Inc., USA) and exported as standard tessellation files (.stl). To avoid damage during the de-build process, specimens were built within a thin protective wall structure (Fig. 1 (a)). Plasma atomised Ti-6Al-4 V (Grade 23) powder feedstock with a size range of 15-53μ m was used to manufacture all samples with a RenAM 500S (Renishaw, UK). Duplicates (n = 10) were prepared for each group with varying laser power and scanning speed (defined as point distance/exposure time for the point-wise scanning of RenAM 500S system) (Table 1). Linear energy density (LED) is calculated from laser power divided by scanning speed to indicate the energy input during manufacturing. Point distance of 45μ m, layer thickness of 30μ m and single contour were constant for all manufactured samples. All specimens were built under an argon atmosphere and on a Ti64 substrate pre-heated to 170 °C. Following manufacture, parts were manually removed while maintaining a final length for all struts of 7 mm.

2.2. Roughness measurement

As-fabricated struts were marked before removing from the plate for roughness measuring of specific interested upper and lower surfaces (Fig. 1 (b)). Images were captured vertically to the sample surface using an optical non-contact profilometer (Alicona Infinite Focus G5, Austria) with a 20 × lens to get the maximum resolution and profile length of ∼ 0.8 mm. Three regions from the up- and down-faces were scanned respectively through top to bottom for each strut. The average roughness (R_a) was obtained by using a Gaussian filter, cut-off wavelength was chosen with a compliance to ISO 4287.

2.3. Micro-CT characterisation

A μ CT system (Skyscan 1172 Bruker, Belgium) was used to investigate the 3D volume of struts. Scans were obtained using a voltage of 80 kV, current of 100 mA, exposure time of 1600 ms, a 0.5 mm aluminium filter, pixel size of 2.44μ m, camera resolution of 2664 × 1120, rotation step of 1.12° and a frame averaging of 6. Cross sections were produced after reconstruction in NRecon (version 1.7.1, Bruker), by which the internal defects generated in the SLM process were detected and exhibited in 3D geometries. Strut thickness was measured at top, middle and bottom section from reconstructed images, then input to ImageJ and averaged for further calculation of mechanical properties and manufacturing accuracy evaluation.

An image analysis method in Fig. 1 (c) was developed to calculate average roughness (R_a) from the complete strut profile captured by μ CT. A threshold of 70 was firstly determined in ImageJ [29] from the reconstructed images by NRecon (version 1.7.1, Bruker) to highlight the solid material. Binary images were then imported to MATLAB (Version R2021b, U.S.A.) and a global threshold of 70 applied. If the pixel grey value was greater than the threshold value, the pixel would be counted to identify the struts solid area, after which the centre of each slice would be located individually by calculating the midpoint of coordinates meeting the condition of threshold over 70. A simple moving average function was used to remove the deviation of eccentricity that may be caused by either poor vertical alignment in the scanner, or overall bends or curvature to the strut. Thus, the current layer was aligned by averaging the centre coordinates for 20 slices forward and backward, respectively. Next, the last pixel within threshold range would be located along the chosen MATLAB angle. By multiplying the given pixel size from μ CT scanning with the number of pixels counted, distance between struts centre and the border were measured and the above steps would be repeated for chosen successive slices to generate the struts profile. At each specific measuring angle, the base line was calculated from the mean value of the measured profile and subtracted to compute the roughness profile, following by R_a calculation as stated in Eq. (1). The overall roughness of each single strut contour was attained by
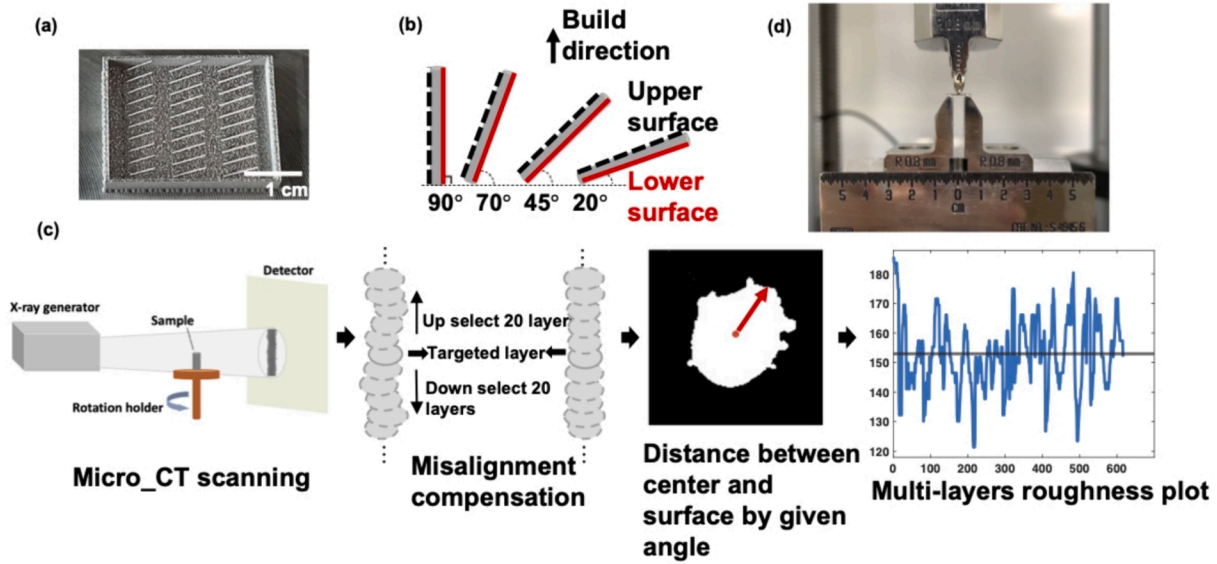
Fig. 1. (a) Image showing the as-built single struts within the protective wall structure; (b) diagram defining the struts angle, upper surface (black-dash marked) and lower surface (red marked); (c) flow diagram displaying the main steps to calculate average roughness of whole strut profile through micro-computed tomography (μ CT) and MATLAB image analysis, and (d) image to illustrate the set up and the beginning position of 3-point bending test. (For interpretation of the references to colour in this figure legend, the reader is referred to the web version of this article.)

Table 1
Design summary of build angles and parameters used in this study.

Strut build angle (°)	Laser power (W)	Exposure time (μ s)	Scan speed (mm/s)	LED (J/mm)
20	100	20	2250	0.04
	150	40	1125	0.13
	200	50	900	0.22
45	100	20	2250	0.04
	150	40	1125	0.13
	200	50	900	0.22
70	100	20	2250	0.04
	150	40	1125	0.13
	200	50	900	0.22
90	100	20	2250	0.04
	150	40	1125	0.13
	200	50	900	0.22

varying the MATLAB measuring angle through 0° to 350° with a 10° interval.

$$R_a = \frac{1}{n}\sum_{i=1}^{n}|y_i| \qquad (1)$$

Where:

n = number of data points in the sampling length.

y_i = absolute value of the difference between the actual height at that point and the mean height of the sampling length.

2.4. Three-Point bending test

Considering the simplicity and adaptivity of specimen preparation and testing, as well as the interests to complex loading mechanism of compression, tension and shearing in lattices, 3-point bending test was conducted on a universal testing machine (Instron 5848, USA) at room temperature, using a 2 kN load-cell [30]. Span length was fixed at 4 mm, displacement rate was set at 0.5 mm/min for all measurements compliant with ASTM E290 (Fig. 1 (d)). Bending continued until failure or if a maximum deformation of 2 mm was reached with independent tests performed on each condition per triplicate. Elastic modulus and maximum flexural strength (MFS) were calculated based on Eq. (2) and

Eq. (3) [31].

$$E_f = \frac{F}{\delta} \bullet \frac{L_{total}^3}{48I} \qquad (2)$$

Where:

F = applied external load, N.

L_{total} = span length or distance between the supporting pins, mm.

δ = deformation, mm.

I = polar moment of inertia, calculated from measured diameter, mm^4.

$$\sigma_f = \frac{F_{max}L_{total}}{4W} \qquad (3)$$

Where:

F_{max} = applied external load at failure, N.

L_{total} = span length or distance between the supporting pins, mm.

W = section modulus, calculated from measured diameter, mm^3.

Average strut diameter used in the equation were obtained from the μ CT reconstructed cross-section area. To acquire a thorough understanding of the failure point, images of the fracture cross-sections were taken with a scanning electron microscope (SEM, Hitachi 3030, Japan).

2.5. In-vitro analysis of osteoblast behaviour on single strut samples

2.5.1. Cell culture

20°, 45° and 70° struts with the LED of 0.13 J/mm were chosen to evaluate the osteoblast cell response. MC3T3 murine pre-osteoblasts were acquired from American Type Culture Collection (ATCC, United Kingdom). Basal medium comprised of minimal essential medium (α-MEM; Sigma-Aldrich, United Kingdom) with 10 % Foetal Bovine Serum, 1 % L-glutamine (Sigma-Aldrich, United Kingdom) and penicillin/streptomycin (Sigma-Aldrich, United Kingdom). Osteogenic medium was prepared by supplementing basal medium with 50 μg/mL L-ascorbic acid (Sigma-Aldrich, United Kingdom) and 10 mM β-glycerophosphate (Sigma-Aldrich, United Kingdom).

The struts were sterilised in 70 % ethanol for 24 h, then washed three times with sterile phosphate buffered saline (PBS, Lonza, United Kingdom) prior to use. For cell seeding, MC3T3s were initially incubated with the CellTracker™ Green CMFDA (2 μM, Thermo Scientific, United

Kingdom) for 30 min in the dark. Following staining, cells were dynamically seeded onto the struts as previously described [13]. Briefly, cell suspension containing 2×10^5 cells were transferred into a sterile 2 ml Eppendorf tube with a hole pierced in the lid. The sterile struts were placed into each tube and the Eppendorf tube sealed with an AeraSeal™ film membrane (Sigma-Aldrich, United Kingdom). The samples were then loaded onto an SB tube rotator (SB3, STUART, United Kingdom) and dynamically cultured for 16 h at 8 rpm (37 °C, 5 % CO_2). The next day, the samples were washed twice with basal medium, then cell adhesion was assessed under an EVOS fluorescent inverted microscope (EVOS M5000, Invitrogen, USA) where the number of cells were quantified. Samples were then incubated in osteogenic media for 21 days with media replaced every two days. After 21 days of culture, cell viability was assessed by live/dead staining. Samples were incubated with basal medium supplemented with CellTracker™ Green CMFDA (2 µM, Thermo Scientific, United Kingdom) and Propidium iodide (1 µg/ml in PBS, Sigma-Aldrich, United Kingdom) for 30 min in the dark. Samples were washed twice with basal medium, then visualised under an EVOS fluorescent inverted microscope (EVOS M5000, Invitrogen, USA).

2.5.2. Alkaline Phosphatase (ALP) activity

ALP activity was quantified using the 4-nitrophenyl colourimetric phosphate liquid assay (pNPP, Sigma-Aldrich, United Kingdom) as previously described [32]. Briefly, 90 µL of pNPP was added to 10 µL of cell lysate (in 0.1 % Triton™ X-100), which was then incubated for 60 min at 37 °C. The absorbance at 405 nm was measured using the SPARK spectrophotometer (TECAN, Switzerland). ALP specific activity (ALPSA) of each sample was calculated using total ALP quantity divided by total DNA content (nM ALP/hr/µg DNA) [33].

2.5.3. DNA quantification

DNA content was quantified by the Quant-iT PicoGreen DNA assay (Invitrogen, Life Technologies, United Kingdom). 10 µL of cell lysate (in 0.1 % Triton™ X-100) was added to 90 µL of TE (10 mM Tris-HCl, 1 mM EDTA) buffer. 100 µL of PicoGreen reagent was added and the fluorescence was read at 480/520 nm using the SPARK spectrophotometer (TECAN, Switzerland).

2.5.4. Collagen production

Collagen deposition was assessed with picrosirius red staining. Samples were washed twice in PBS then fixed in 10 % neutral buffered formalin (NBF, Cellpath, United Kingdom) for 30 min. Following which samples were stained with Picro-Sirius Red Solution (ScyTek Laboratories, Inc., USA) for 1 h. The samples were washed in 0.5 M acetic acid followed by distilled water and then air dried. For the quantification of collagen staining, 0.5 M sodium hydroxide was was added to elute the bound dye and absorbance was measured at 590 nm using a SPARK spectrophotometer (TECAN, Switzerland). Collagen production was normalised with DNA content.

2.5.5. Calcium deposition

Alizarin red staining was conducted to evaluate calcium deposition. Briefly, cells were washed with PBS then fixed in 10 % NBF (Cellpath, United Kingdom) for 30 min. Samples were washed in distilled water and then incubated with alizarin red solution (Sigma-Aldrich, United Kingdom) for 10 min. Following staining, samples were washed with distilled water. For the quantification of alizarin red staining, stained samples were eluted with 10 % cetylpyridinium chloride (Sigma-Aldrich, United Kingdom) for 1 h and then absorbance measured at 550 nm in the SPARK spectrophotometer (TECAN, Switzerland). Calcium content was normalised with DNA content.

2.6. Statistics

All statistical analysis was conducted using Prism (GraphPad Software, version 9.0.0, USA). Two-way ANOVA was performed followed by Tukey's post-hoc to reveal the effects of process parameters and build angles on Ti64 struts. Alpha level was 0.05, p values lower than or equal to which were deemed significant. *P < 0.05, **P < 0.01, ***P < 0.001, ****P < 0.0001. Results are shown as average ± standard deviation.

3. Results

3.1. Effect of process parameters and struts angle on geometric defects

The porosity was evaluated by both the open pores (op) connected to the strut surface and internal closed pores (cl) which are enclosed by solid material, both of which were captured by µ CT (Fig. 2 **(a)**). Specimens built at the lowest LED of 0.04 J/mm were largely hollow showing a significant lack of fusion in their core that seems to decrease as the strut angle increases with the open porosity of samples built at 20° and 45° greater than the 70° and 90° struts. Spheroidization could be observed at the surface and inter-layers of the struts which may be caused due to balling during manufacturing. As the LED increases, both the internal closed and open porosity rapidly decreases with struts manufactured using a LED of 0.13 J/mm fully melted, ∼ 0 %, across all struts angles. Further increases in LED, 0.22 J/mm, revealed struts dominated by isolated closed pores, shown as gas pores or keyholes, especially noticeable in 90° struts that showed higher porosity compared with those built at 70° and lower where porosity remained below 1 %.

The actual sturts thickness of all specimens is shown in Fig. 2 (b), where it can be clearly seen that the struts thickness increases with the LED. The standard deviation (SD) is relative larger for LED of 0.04 J/mm. Struts manufactured by 0.13 J/mm showed the highest accuracy with an average thickness of 257.8 ± 13.2µ m. Noticeably, for the same LED, the struts thickness appears to be decreasing as the struts angle increases.

3.2. Effect of process parameters and struts angle on average roughness

Average roughness R_a of upper and lower areas of the strut was shown to be influenced differently by process parameters and struts angle (Fig. 3). The upper surface shows a general decrease in roughness with increased LED for all angles considered, albeit only significantly different for the 20° sample (p < 0.01) (Fig. 3 (a)). As presented in Fig. 3 (b), the upper R_a for struts produced at 0.13 J/mm and 0.22 J/mm for 20°(9.5 ± 1.6µ m and 10.4 ± 2.0µ m) was shown to be smoother than the struts of 0.04 J/mm (19.4 ± 4.2µ m). These surfaces also seem to be affected by lower struts angle resulting in rougher surfaces than struts ≥ 45°. On the other hand, the lower areas of the struts appear to raise their average roughness with increased energy density for struts ≤ 45°. Similarly, to the upper surfaces, it should be noticed that the R_a of struts angle of 20° was significantly greater than those above 45° at LED of 0.22 J/mm (Fig. 3 (a)). The lower surface of 20° struts were largely covered by partially melted powder with wavier surfaces observed as the LED increases in Fig. 3 (b), opposite to the upper surfaces while struts processed under the same LED.

The R_a obtained through image analysis in Fig. 3 (c), reveals values between 10µ m and 15µ m, for strut angles above 45° which are in line with the measurements observed with optical profilometry Fig. 3 (a). Similarly, the R_a of 20° drastically increased as the LED was risen for the lower surface, which agrees with the R_a measurements. Roughness appears to be more uniform for strut angles above 45°, while as LED increases, the R_a map of 20° struts tend to be more elliptic. Notably, for struts manufactured by 0.13 J/mm, R_a reached the lowest value of 9.0 ± 1.9µ m for 45°, 7.9 ± 1.8µ m for 70°, and 7.6 ± 1.4µ m of 90°.

3.3. Effect of process parameters and struts angle on mechanical properties

In Fig. 4 (a) and (b), there is a general increase in maximum flexural strength (MFS) and elastic modulus as the LED increases from 0.04 J/
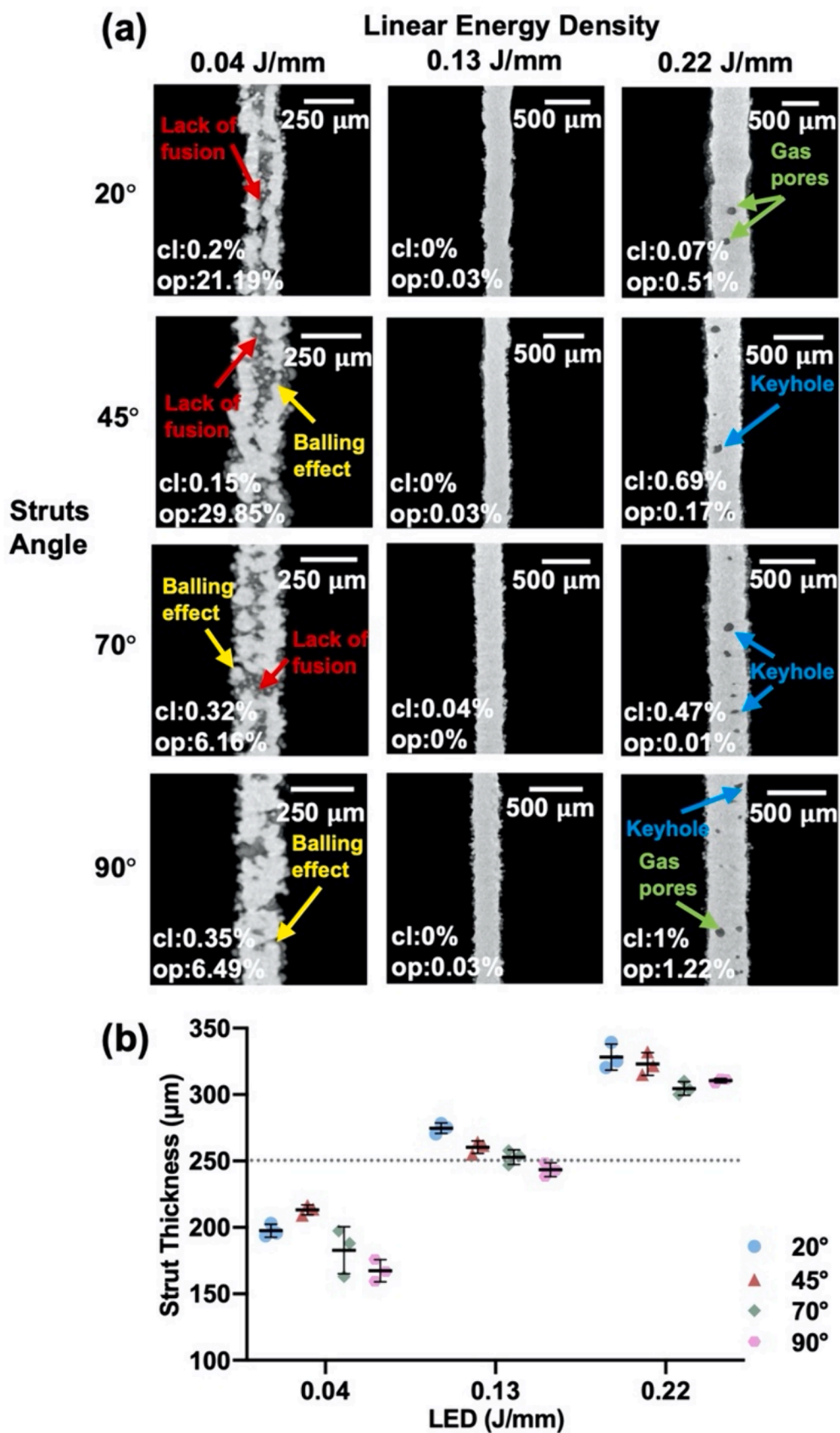
Fig. 2. (a) Images showing inner morphology of struts scanned by µ CT, where defects are indicated by arrows for lack of fusion, balling effect, gas pores and keyholes, porosity including open and internal closed is shown at the bottom left of each image; (b) actual struts thickness varies with different LED for all specimens (n = 3, shown as mean ± SD).
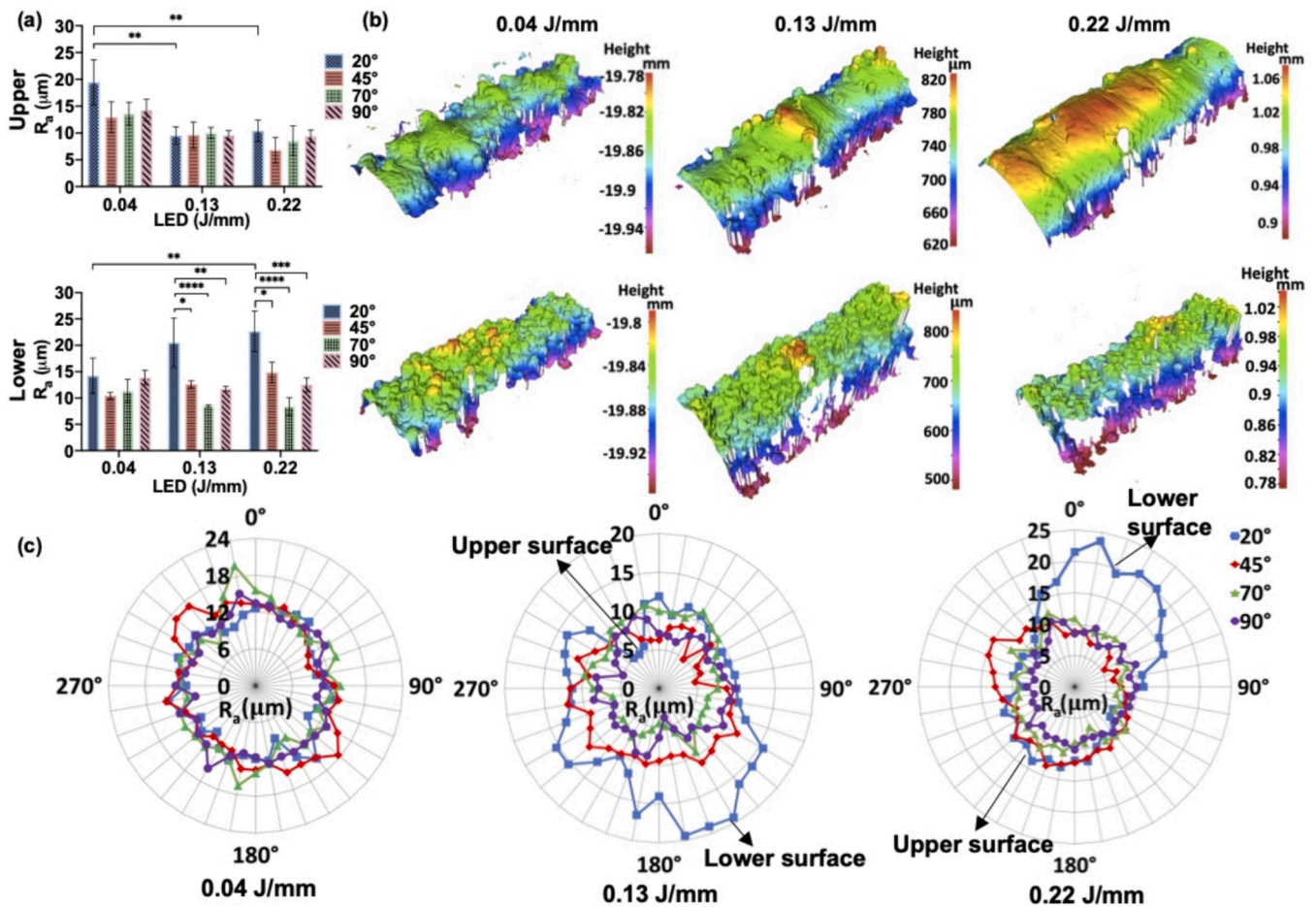
Fig. 3. Plot showing the build angles and process parameters effects on (a) upper and lower surface of struts; (b) 3D maps presenting the upper and lower surface of 20° struts built with 0.04 J/mm, 0.13 J/mm, and 0.22 J/mm energy densities; (c) radar figures showing whole profile of R_a, plotted against measured angle in MATLAB for single strut built with different LED, as well as showing recognisable upper and lower area of 20°.

mm to 0.13 J/mm. Further increase in LED only improved the mechanical properties of the 20° strut with 45° and 70° remaining largely unchanged and 90° displaying a slight reduction. These properties seem to display trends highly correlated with the build angle, with positive relationships apparent for lower LED, 0.04 J/mm, negative arising for the higher LED studied, 0.22 J/mm, and stagnation at 0.13 J/mm.

Fig. 4 (c-f) shows typical stress–strain curves of the 3-point bending tests on struts; firstly, a linear region of elastic gradient, secondly a region of plastic deformation following the yield point, and finally an irregular region prior to failure. For struts built at 0.04 J/mm, all failed immediately after reaching the MFS (Fig. 4 (c)) while, as the LED increased to 0.13 J/mm, struts above 45° showed a smooth plateau region until achieving a 2 mm deformation suggesting a more ductile behaviour (Fig. 4 (d)). For the 0.22 J/mm struts, two different phenomena were observed. Those above 45° either experienced a direct failure after MFS (Fig. 4 (e)) or entered a non-failure plateau region (Fig. 4 (f)).

Struts built at 20° all ruptured by crack propagation regardless of process parameters (Fig. 5 (a)), where the failed samples showed crack propagation along a zigzag path. No cracks or fracture were found for struts above 45° processed at 0.13 J/mm. Where cracks can be clearly seen on the struts, 0.22 J/mm specimens that ruptured after plastic deformation displayed a notable pore pit at the fracture surface, except those manufactured at 20° (Fig. 5 (b)). These pores were surrounded by smooth and concentric shapes and displayed rough fracture surfaces. (Fig. 5 (b)) shows secondary electron micrographs of the fracture surface featuring notable dimples and voids, suggesting a ductile behaviour of

the 0.22 J/mm manufactured struts.

3.4. Effect of process parameters and struts angle on in-vitro osteoblast response

Following dynamic seeding of the struts, cellular adhesion was visualised by fluorescent microscopy. Viable cells could be seen distributed throughout the struts surface in all groups (Fig. 6 (a)). The 20° struts exhibited increased quantity of cells towards the edge of the struts, whilst cell distribution was more homogenous in the 45° and 70° struts. Quantification of the images in Fig. 6 (c) confirmed that 20° struts exhibited a significant increase in cell attachment when compared to the 45° and 70° struts. These findings are likely due to the increased roughness exhibited by the 20° struts which likely correlates to increased cell adhesion at early time points. Following 21 days of osteogenic culture, live/dead staining showed that cells on the struts were highly viable and reached confluency in all groups (Fig. 6 (b)).

To investigate the influence of the different strut fabrication angles on osteogenic differentiation, alkaline phosphatase (ALP) activity, collagen production and calcium deposition were evaluated. Initially, ALP activity, an early marker of osteogenesis, was evaluated following 14 days in osteo-inductive culture. The findings in Fig. 6 (d) showed significantly enhanced ALP levels within the 20° groups when compared to the 45° and 70° struts ($p \leq 0.01$). Picrosirius red staining showed that the 20° struts exhibited a significant increase in collagen content when compared to the 45° ($p \leq 0.05$) and 70° struts ($p \leq 0.01$) (Fig. 6 (e)). Similarly, in Fig. 6 (f) alizarin red staining for calcium deposition
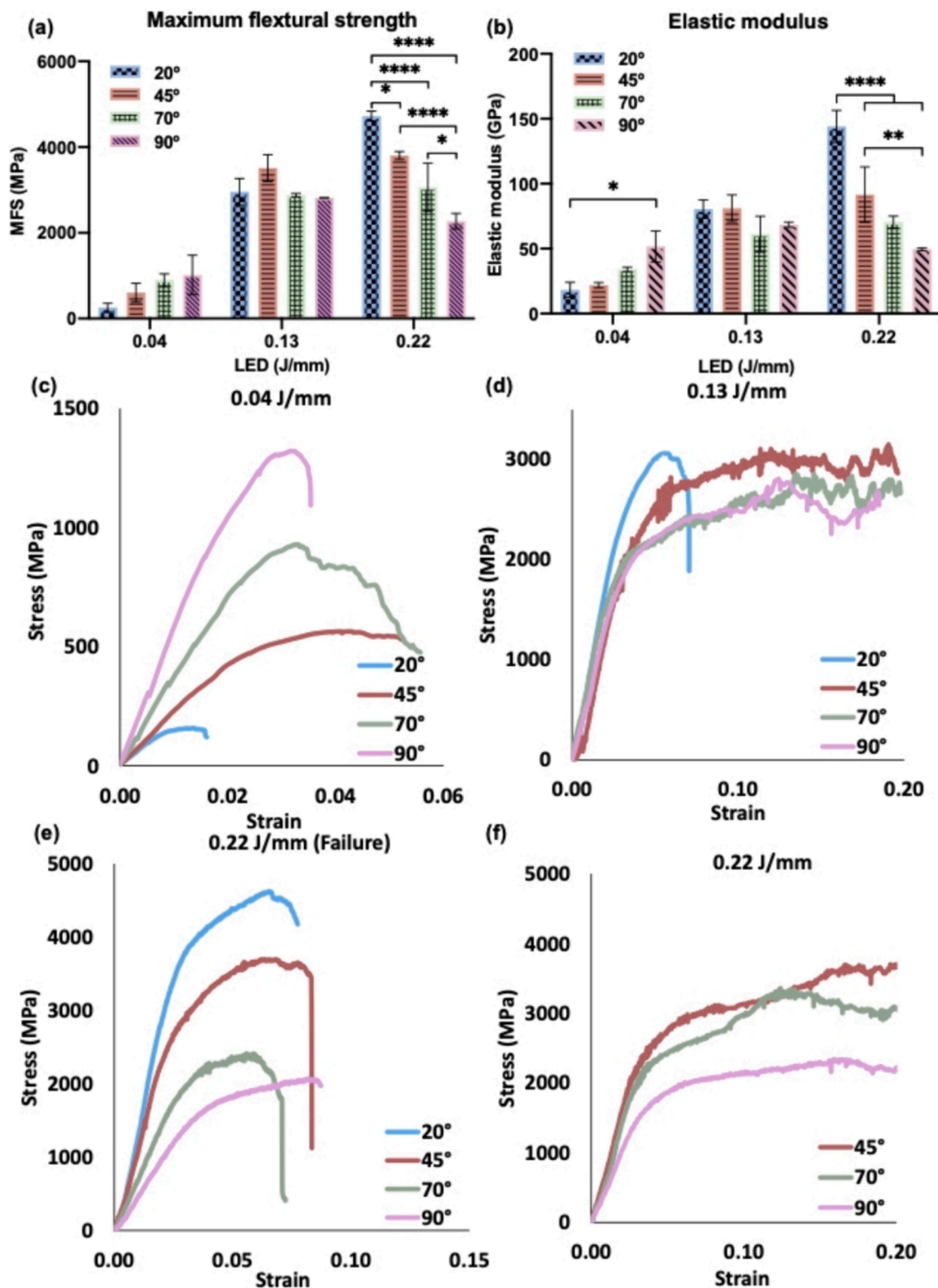
Fig. 4. 3-point bending results showing build angle effects for (a) MFS and (b) elastic modulus of struts; force–displacement curve taken at different LED of (c) 0.04 J/mm, (d) 0.13 J/mm, 0.22 J/mm for (e) failure occurred and (f) without failure.

showed that the 20° and 45° struts exhibited substantial increase in calcium deposition when compared to the 70° group (p ≤ 0.05). The osteogenic differentiation induced by these different struts clearly shows that reducing the struts angle enhances the osteogenic capacity of cells on these materials. This is likely attributed to the increased roughness observed on these lower tilted struts, as several studies have indicated

the influence of roughness on osteo-induction.

4. Discussion

The occurrence of lack of fusion (Fig. 2 (a)) in struts built at 0.04 J/mm LED can be attributed to insufficient laser energy input, resulting in
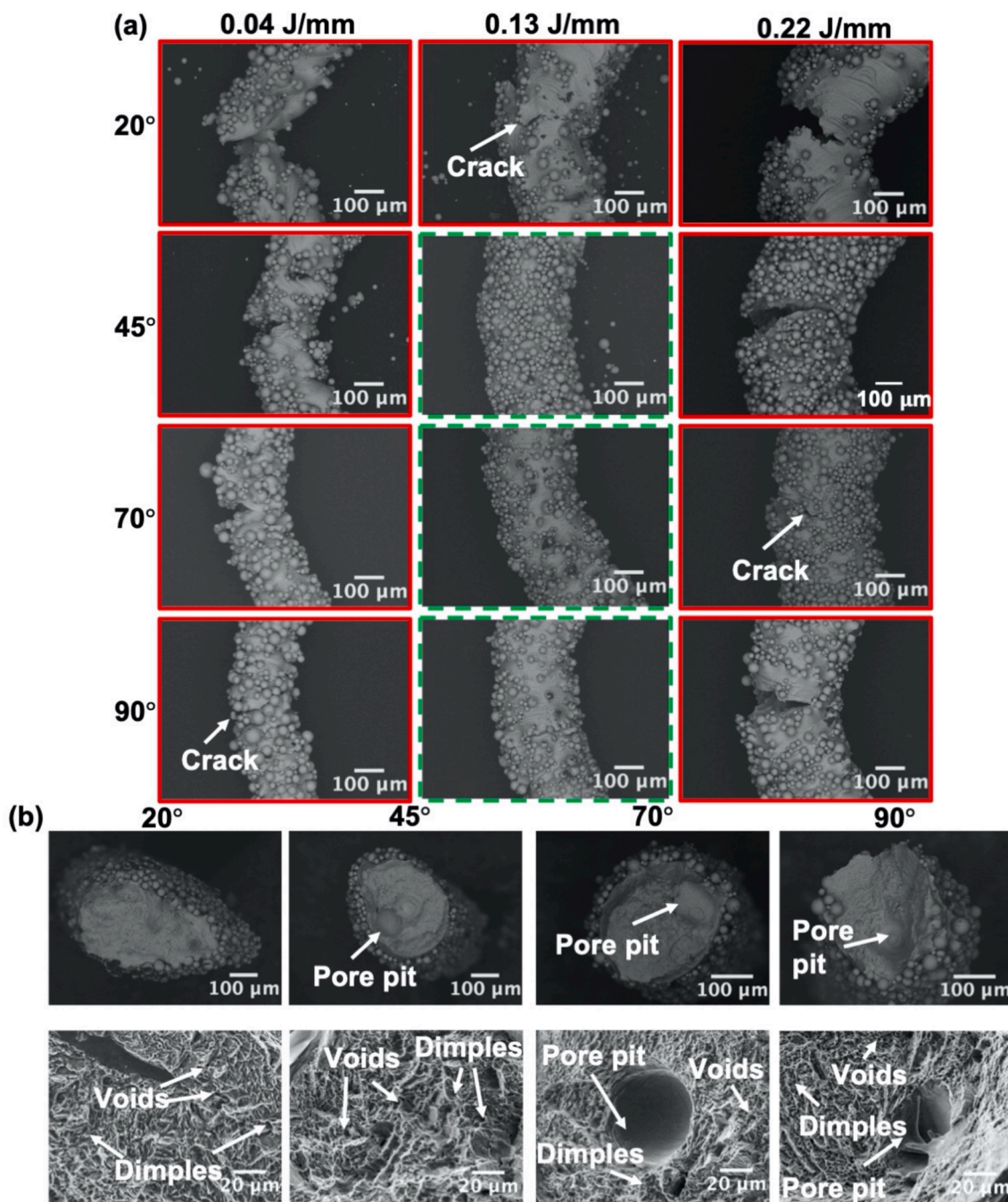
Fig. 5. Images showing fabricated struts (a) failure in red solid frame and without failure in green dashed frame after bending test; (b) showing cross-section of 0.22 J/mm manufactured struts after failure occurred to illustrate the ductile topography of Ti64 struts. (For interpretation of the references to colour in this figure legend, the reader is referred to the web version of this article.)

un-melted powder particles existing between the adjacent melted regions [34]. Lack of fusion tends to be more obvious and severe as struts angle decreasing, due to the larger powder area left un-melted by a low laser energy input. Balling effect fusion (Fig. 2 (a)), resulting from poor wettability is also reported to be more prevalent under low energy density conditions as a resulting in spheroidization and discontinuity of the melt pool [18] alongside poor bonding between layers. At higher LED (0.22 J/mm), escaping material vapour during melting leads to keyhole formation and subsequent porosity following its collapse [35]. Besides, the vertically aligned melt pool between layers of 90° possibly leads to the repeating deposited materials experiencing more intense and frequent heat of laser compared to lower struts angle (Fig. 2 (a)).

This effect of heat accumulation generated as a results of multiple re-melting might increase the porosity for 90° struts [36].

At low LED, lack of fusion and balling would be the main factors increasing R_a. These defects not only create an inherent roughness due to introducing discontinuity of material, but they also disrupt the uniform deposition of subsequent powder layers [20]. Process conditions could play a more important role on the roughness profile at this low LED stage than strut angle, leading to the poor melting of materials regardless of geometric angle (Fig. 3 (a) and (c)). Whilst as the LED increases, so too does melt pool depth and width which may improve inter-layer bonding and remelting of surface adhered particles. On the other hand, because of loose powders largely distributed at the lower surface as the struts
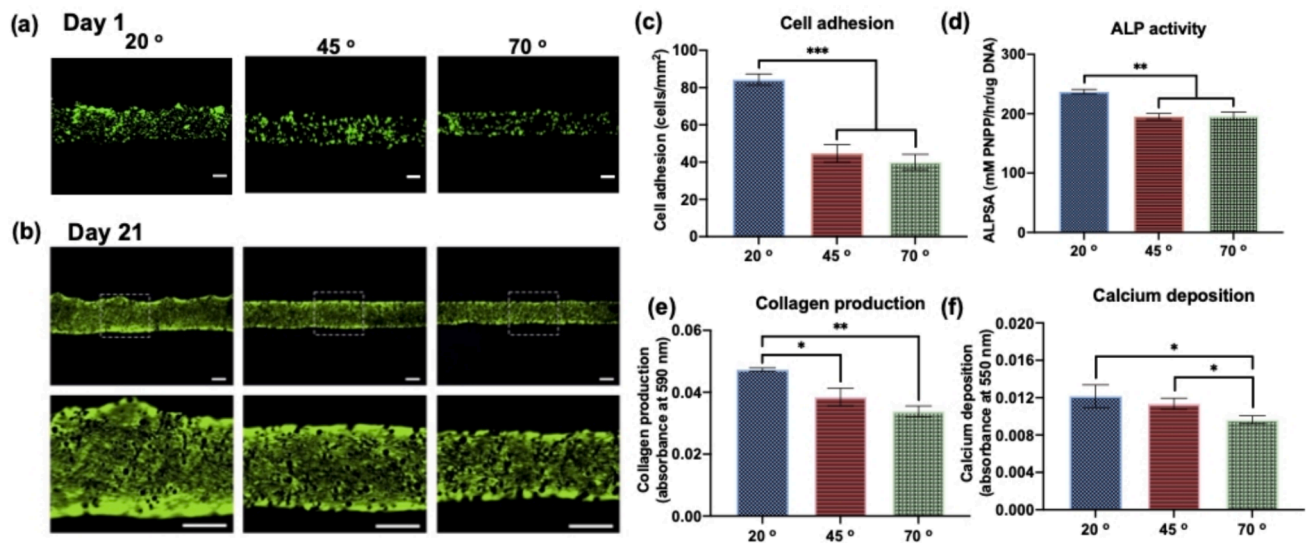
Fig. 6. Microscopy images showing live cell adhesion on struts surface for (a) day 1 and (b) live/dead cell staining after 21-days culture, plots illustrating (c) cell adhesion, (d) ALP activity, (e) collagen production and (f) calcium deposition on 20° to 70° struts, scale bar represented 200 μm for all.

angle decreases, poor heat conduction would expand the formation of overhang for low-angle struts [19]. Surface irregularities could be more observable as the increasing LED causes formation of wider and deeper melt pool, therefore larger sintering of raw materials, leading to greater R_a of lower surface (Fig. 3 (b)).

The failure of 3-point bending test samples occurred in all specimens when applying the lowest LED with insufficient energy input resulting in high porosity generated by lack of fusion. The large size and irregular shape of these pores may act as stress concentration and subsequent crack initiation points which leads to weak load-bearing capacity, impacting both mechanical strength and stiffness [37]. As LED increases, enhanced ductility for struts above 45° indicates the importance of optimising parameters for elimination of enclosed pores. For struts manufactured with LED 0.22 J/mm, the failure mode of all the specimens agreed with the study of Paulo et al. and Costanzo et al [38,39]. At the highest LED, the increased porosity for higher angle struts due to keyhole and gas pore defects (especially for 90° struts) may be a critical factor in reducing strength and elastic modulus. The pore pit located at the fracture point for struts above 45° are considered as stress concentration risers, which can cause the struts to fail under relatively low level of stress, inducing the failure and propagating to the surrounding solidified region [40]. Moreover, the strut angle and as-built strut thickness tends to result in the dramatic changing of the UFS and elastic modulus (Fig. 2 (b) and Fig. 4 (b)). It has been found that part heat accumulation depends on build angle, leading to the variation of both mechanical properties and internal porosity [41]. Consistent with the phenomena in this work, it was demonstrated by Palmeri et al. that the Ti64 samples built above 45° exhibited lower mechanical strength and higher ductility than the samples built below 45°. These findings were associated with an increasing heat accumulation due to the larger volume of the solidified materials and number of layers, that below the depositing layer of higher struts angles. Furthermore, as Barba et al. observed that the microstructure could be influenced by the changing of strut size and build orientation, which could potentially cause differences in elastic modulus [42]. It can also be assumed that the failure occurrence was associated with average roughness. The high R_a of 20° struts lower surface can influence the mechanical performance of SLM lattices by creating stress concentrations or microcracks at the peaks and valleys of the rough surface and reducing the overall ductility of the part. This phenomenon corresponds with the results observed by Scott et al., indicating that the higher roughness would be more detrimental to mechanical properties of components, causing earlier strain (work)-to-

failure [43]. As explained, struts above 45° manufactured by LED of 0.13 J/mm which showed the lowest R_a. Therefore, struts could be less distorted, uniformly melted and solidified, ensuring a more consistent microstructure and stable mechanical properties throughout the part.

There is a growing body of evidence demonstrating the influence of mechanobiological interactions between cells and their substrates on directing cell behaviour [13,44]. The substrates surface roughness has been proved to critically influence cell response [45]. At optimised process parameters, osteoblasts were shown to preferably adhere to and proliferate on as-build struts of lower angle below 45°. The results of cell adhesion in Fig. 6 (c) fit with the changing of lower-surface R_a in Fig. 3 (a), indicating that a rougher surface is probably a positive factor to enhance initial contact between the implant and cells, a critical process for successful osseointegration. In addition to the initial cell adhesion, several studies have demonstrated the role of substrate roughness on improved osteogenic differentiation via the activation of mechano-transducive signalling [46,47]. In the present study, we observed that the rougher surfaces also facilitated osteoblast collagen production and calcium deposition. This suggests that the selection of struts angle is extremely important for the initial cell behaviour and the subsequent osseointegration process. Meanwhile, the attached partially melted powders were not shown to be covered by cells, emphasising the importance of eliminating these particles during post processing. These observations are in line with the work of Cox et al., where the relatively large angle between partially melted particles and the solid surface might block the spread of cells [45].

With the idea of improving implant mechanical and biological properties whilst controlling the manufacturing process, a map was developed to guide the design of AM lattices. Fig. 7(a) defined the angle α and α′ used to calculate the struts angle assembled in a BCC lattice. Starting from either adjusting build orientation of lattices, θ, Fig. 7(b) or adjusting the unit cell size (height) Fig. 7(c), the build angle of individual strut α^*, α^{**} and γ in the lattice can be customised. As the gradient colour maps of Fig. 7(d) & (e) indicate, struts built lower than 45° display improved osteoblast cell adhesion but poor mechanical performance (green), while struts built above 45° show an opposite behaviour (red) with a superior ductility but reduced cell response. Overall, 45° struts built with LED of 0.13 J/mm showcase superior properties in both mechanical strength and osteoblast behaviour than other struts. The deviation from 45° was thus calculated by Eq. (4) and Eq. (5), which can be used as an indicator to determine the actual build angle of struts in a rotated or unit cell size changed lattice.
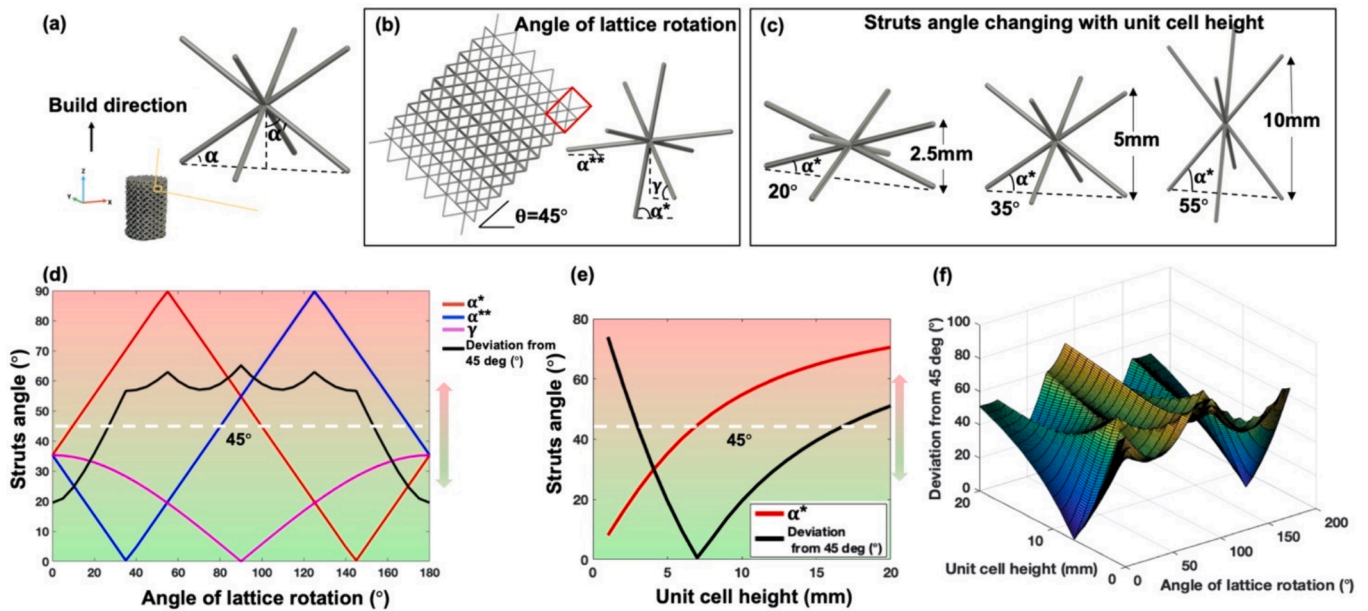
Fig. 7. (a) BCC unit cell showing the angles used for the determination of actual strut angle after lattice rotation and unit cell height changing; (b) showing an example of unit cell orientated when rotating a lattice to angle of $\theta = 45°$, α^*, α^{**} and γ indicate the actual build angle of struts (c) presenting the difference of struts angle after the unit cell height adjusted; (d) illustrating struts angle being manufactured in a rotated lattice, whilst (e) plotting the build angle of struts when unit cell height changes; up-down arrows indicate areas for enhanced ductility but poor cell attachment (red) or improved cell adhesion but reduced ductility (green); (f) map illustrating the deviation of struts angle from 45° while rotating the lattices and adjusting the unit cell height. (For interpretation of the references to colour in this figure legend, the reader is referred to the web version of this article.)

$$\text{Deviation from } 45° = \sqrt{(\alpha^* - 45°)^2 + (\alpha^{**} - 45°)^2 + 2*(\gamma - 45°)^2} \quad (4)$$

$$\text{Deviation from } 45° = 2*|(\alpha^* - 45°)| \quad (5)$$

Struts angle against lattice rotation in Fig. 7 (d) can be used to select the orientation of a preferred BCC unit cell in a selected geometry, assisting further design and property modification of the whole part. Meanwhile, Fig. 7 (e) showcases a design map to modify a lattice with fixed orientation . These two approaches can be combined to enable full tailoring of unit cell height and/or part build orientation to optimise geometry of lattices (Fig. 7 (f)). Furthermore, these could be adapted depending on specific needs on an implant.

The ideal and key properties of porous metallic implants include biocompatibility, comparable mechanical strength and stiffness, surface morphology facilitating cell attachment, proliferation, differentiation and migration [48]. For biomedical devices requiring load bearing, it is critical to avoid mechanical failure while maintaining suitable mechanical strength of implants to patients' bone, which is further challenged by different bone conditions, such as quality, density, and disease location of bone [49]. The representative 3-point bending results suggest that lattice struts manufactured above 45° have exceptional ductility without failure, plus a wide range of strength between 2811 MPa to 3715 MPa that could be tailored into porous implants to meet various personalisation requirement. Mechanical strength and elastic modulus could be adjusted through either rotating lattice or varying unit cell height, therefore, by containing more, or less struts above 45° to accommodate broader bone implants application.

When bone defect exceeds the size limit (approximately > 2 cm) of bone self-regeneration, implantable lattices with surface quality satisfying bone cell response are essential to promote initial bone ingrowth effectively. In this study, it is demonstrated that AM processed struts with different topological features could significantly influence mammalian cell behaviour, where the struts built below 45° possess an outstanding performance on bone cell attachment, proliferation, and differentiation. This work created the map to allow users to select lattices with precise control of surface finish to improve bone regeneration

process [27]. The map with the customisation function of combining the mechanical and surface morphology features, could be particularly applicable as new-generation bone substitute for bone defects repair caused by trauma, tumour, or functional atrophy [50]. In the future, it is also essential to explore the optimal build orientation of whole lattices regarding to the map. De Biasi et al. has proposed and verified a cost-efficient way to utilise struts and nodes built with different orientations to predict and improve the fatigue of lattice structures through algorithm driven by experimental results [51]. Further utilizations of the map to design optimal *meta*-biomaterials has been taken into account by the authors, to conduct evaluation and verification by combining simulation and experimental work.

Moreover, given the highly complex and fine geometry features of lattices, common post-processing, such as sand blasting, would be extremely difficult to complete for these geometries. Thus, this approach could also be potentially useful to select part build orientation and/or unit cell height to alter and predict surface quality, conducting further post-process, rendering higher efficiency for research community, engineers, AM users and clinicians.

5. Conclusions

To improve of the osseointegration ability of Ti64 porous medical devices, this study explored the effect of process parameters and struts angle on surface quality, mechanical properties, and cell response of lattice struts. From the presented results, it was observed that both laser energy input and design properties heavily influenced the behaviour of the final product. For struts built at optimised LED of 0.13 J/mm, all parts were fully melted with those above 45° exhibiting greater ductility without obvious failure. For strut angles below 45°, mammalian cells showed the preference of attachment, proliferation, and mineralisation to the overall rougher surface comparing to struts built higher than 45°. However, a less ductile behaviour from 3-point bending test was observed at low struts angle. An image analysis method was developed to detect the whole profile roughness of struts and promised to be an effective way to represent and predict the surface quality of complex

lattice structure.

Combining these findings, by using 45° as a reference and BCC lattice as a representative demonstrator, processing maps were developed to take advantage of part rotation and unit cell design to optimise complex AM structures. As a design-assistance map, the final output would enable functionalisation of these parts during the early manufacturing stages for improved mechanical and/or cell behaviour. Thus, it will be possible to predict and modify the properties of SLM latticed structures in-situ, increasing the confidence and applicability of these techniques for all AM stakeholders, and healthcare professionals while also improving the outcomes of medical devices.

CRediT authorship contribution statement

Xue Cao: Writing – original draft, Software, Methodology, Investigation, Data curation, Conceptualization. **Luke N. Carter:** Conceptualization, Methodology, Software, Supervision, Writing – review & editing. **Kenny Man:** Writing – review & editing, Writing – original draft, Methodology, Data curation. **Victor M. Villapún:** Software, Writing – review & editing. **Lucie Giangiorgi:** Writing – review & editing, Software. **Sophie C. Cox:** Conceptualization, Funding acquisition, Project administration, Supervision, Writing – review & editing.

Declaration of competing interest

The authors declare that they have no known competing financial interests or personal relationships that could have appeared to influence the work reported in this paper.

Data availability

Data will be made available on request.

Acknowledgements

References

[1] N. Koju, S. Niraula, B. Fotovvati, Additively manufactured porous Ti6Al4V for bone implants: a review, Metals 12 (4) (2022).

[2] R.S. Sumant Ugalmugle, Orthopedic Devices Market Size, By Product (Joint Reconstruction Devices {Hip Replacement, Knee Replacement, Ankle Replacement, Shoulder Replacement}, Spinal Devices, Trauma Fixation Devices, Ortho biologics, Arthroscopic Devices), Industry Analysis Report, Regional Outlook, Application Potential, Competitive Market Share & Forecast, 2023 – 2032, Global Market Insights, 2022, p. 180.

[3] S. Kedia, R.K. Chaurasia, A.K. Satpati, R.K. Chittela, A.V.S.S.N. Rao, B.K. Sapra, J. P. Nilaya, Effect of laser fluence and pulse overlapping on corrosion properties, cytocompatibility and osseointegration of Ti6Al4V Alloy, J. Mater. Sci. 59 (1) (2023) 228–242.

[4] T. Kluter, H. Hassan, A. Rasch, H. Naujokat, F. Wang, P. Behrendt, S. Lippross, L. Gerdesmeyer, D. Eglin, A. Seekamp, S. Fuchs, An Ex Vivo Bone Defect Model to Evaluate Bone Substitutes and Associated Bone Regeneration Processes, Tissue Eng. Part C Methods 26 (1) (2020) 56–65.

[5] R. Huiskes, H. Weinans, B. Vanrietbergen, The Relationship between Stress Shielding and Bone-Resorption around Total Hip Stems and the Effects of Flexible Materials, Clinical Orthopaedics and Related Research (274) (1992) 124–134.

[6] W. Liu, L. Zheng, C. Wang, H. Yin, A. Raffaella, A. Apicella, P. Ji, H. Zhang, Y. Fan, Additively manufactured bioceramic scaffolds with 3D architecture for vertical bone augmentation: A proof-of-concept study, Mater. Des. 239 (2024).

[7] D.S.J. Al-Saedi, S.H. Masood, M. Faizan-Ur-Rab, A. Alomarah, P. Ponnusamy, Mechanical properties and energy absorption capability of functionally graded F2BCC lattice fabricated by SLM, Mater. Des. 144 (2018) 32–44.

[8] J. Kadkhodapour, H. Montazerian, A. Darabi, A.P. Anaraki, S.M. Ahmadi, A. A. Zadpoor, S. Schmauder, Failure mechanisms of additively manufactured porous biomaterials: Effects of porosity and type of unit cell, J. Mech. Behav. Biomed. Mater. 50 (2015) 180–191.

[9] J. Wieding, A. Jonitz, R. Bader, The Effect of Structural Design on Mechanical Properties and Cellular Response of Additive Manufactured Titanium Scaffolds, Materials 5 (8) (2012) 1336–1347.

[10] M. Mazur, M. Leary, M. McMillan, S. Sun, D. Shidid, M. Brandt, Mechanical properties of Ti6Al4V and AlSi12Mg lattice structures manufactured by Selective Laser Melting (SLM), Laser Additive Manufacturing: Materials, Design, Technologies, and Applications (88) (2017) 119–161.

[11] D. Barba, E. Alabort, R.C. Reed, Synthetic bone: Design by additive manufacturing, Acta Biomater. 97 (2019) 637–656.

[12] H.E. Burton, N.M. Eisenstein, B.M. Lawless, P. Jamshidi, M.A. Segarra, O. Addison, D.E.T. Shepherd, M.M. Attallah, L.M. Grover, S.C. Cox, The design of additively manufactured lattices to increase the functionality of medical implants, Mater Sci Eng C Mater Biol Appl 94 (2019) 901–908.

[13] K. Man, M.Y. Brunet, S. Louth, T.E. Robinson, M. Fernandez-Rhodes, S. Williams, A.S. Federici, O.G. Davies, D.A. Hoey, S.C. Cox, Development of a Bone-Mimetic 3D Printed Ti6Al4V Scaffold to Enhance Osteoblast-Derived Extracellular Vesicles' Therapeutic Efficacy for Bone Regeneration, Front. Bioeng. Biotechnol. 9 (2021) 757220.

[14] L.N. Carter, O. Addison, N. Naji, P. Seres, A.H. Wilman, D.E.T. Shepherd, L. Grover, S. Cox, Reducing MRI susceptibility artefacts in implants using additively manufactured porous Ti-6Al-4V structures, Acta Biomater. 107 (2020) 338–348.

[15] Q. Wang, M. Gao, Q. Li, C. Liu, L. Li, X. Li, Z. Liu, A Review on Energy Consumption and Efficiency of Selective Laser Melting Considering Support: Advances and Prospects, International Journal of Precision Engineering and Manufacturing-Green Technology 11 (1) (2023) 259–276.

[16] A.N. Aufa, M.Z. Hassan, Z. Ismail, Recent advances in Ti-6Al-4V additively manufactured by selective laser melting for biomedical implants: Prospect development, J. Alloy. Compd. 896 (2022).

[17] T. Maconachie, M. Leary, B. Lozanovski, X.Z. Zhang, M. Qian, O. Faruque, M. Brandt, SLM lattice structures: Properties, performance, applications and challenges, Mater. Des. 183 (2019).

[18] H. Salem, L.N. Carter, M.M. Attallah, H.G. Salem, Influence of processing parameters on internal porosity and types of defects formed in Ti6Al4V lattice structure fabricated by selective laser melting, Mater. Sci. Eng. A 767 (2019).

[19] A. Charles, A. Elkaseer, L. Thijs, V. Hagenmeyer, S. Scholz, Effect of Process Parameters on the Generated Surface Roughness of Down-Facing Surfaces in Selective Laser Melting, Appl. Sci. 9 (6) (2019).

[20] C. Qiu, S. Yue, N.J.E. Adkins, M. Ward, H. Hassanin, P.D. Lee, P.J. Withers, M. M. Attallah, Influence of processing conditions on strut structure and compressive properties of cellular lattice structures fabricated by selective laser melting, Mater. Sci. Eng. A 628 (2015) 188–197.

[21] D. Greitemeier, C. Dalle Donne, F. Syassen, J. Eufinger, T. Melz, Effect of surface roughness on fatigue performance of additive manufactured Ti–6Al–4V, Mater. Sci. Technol. 32 (7) (2016) 629–634.

[22] Z. Wang, Z. Xiao, Y. Tse, C. Huang, W. Zhang, Optimization of processing parameters and establishment of a relationship between microstructure and mechanical properties of SLM titanium alloy, Opt. Laser Technol. 112 (2019) 159–167.

[23] S.M. Ahmadi, R. Hedayati, R.K. Ashok Kumar Jain, Y. Li, S. Leeflang, A.A. Zadpoor, Effects of laser processing parameters on the mechanical properties, topology, and microstructure of additively manufactured porous metallic biomaterials: A vector-based approach, Mater. Des. 134 (2017) 234–243.

[24] S. Murchio, M. Dallago, F. Zanini, S. Carmignato, G. Zappini, F. Berto, D. Maniglio, M. Benedetti, Additively manufactured Ti-6Al-4V thin struts via laser powder bed fusion: Effect of building orientation on geometrical accuracy and mechanical properties, J. Mech. Behav. Biomed. Mater. 119 (2021) 104495.

[25] M. Mazur, M. Leary, S. Sun, M. Vcelka, D. Shidid, M. Brandt, Deformation and failure behaviour of Ti-6Al-4V lattice structures manufactured by selective laser melting (SLM), Int. J. Adv. Manuf. Technol. (2015).

[26] U. Hossain, S. Ghouse, K. Nai, J.R.T. Jeffers, Mechanical and morphological properties of additively manufactured SS316L and Ti6Al4V micro-struts as a function of build angle, Addit. Manuf. 46 (2021) 102050.

[27] V.M. Villapún, L.N. Carter, N. Gao, O. Addison, M.A. Webber, D.E.T. Shepherd, J. W. Andrews, M. Lowther, S. Avery, S.J. Glanvill, L.M. Grover, S.C. Cox, A design approach to facilitate selective attachment of bacteria and mammalian cells to additively manufactured implants, Addit. Manuf. 36 (2020).

[28] J.T. Ho, J. Wu, H.L. Huang, M.Y. Chen, L.J. Fuh, J.T. Hsu, Trabecular bone structural parameters evaluated using dental cone-beam computed tomography: cellular synthetic bones, Biomed. Eng. Online 12 (2013) 115.

[29] C.A. Schneider, W.S. Rasband, K.W. Eliceiri, NIH Image to ImageJ: 25 years of image analysis, Nat. Methods 9 (7) (2012) 671–675.

[30] C.C. Chamis, Analysis of the three-point-bend test for materials with unequal tension and compression properties, National Aeronautics and Space Administration (1974) 33.

[31] tec-science, Bending flexural test, 2018. https://www.tec-science.com/material-science/material-testing/bending-flexural-test/.

[32] K. Man, C. Alcala, N.V. Mekhileri, K.S. Lim, L.H. Jiang, T.B.F. Woodfield, X. B. Yang, GelMA Hydrogel Reinforced with 3D Printed PEGT/PBT Scaffolds for Supporting Epigenetically-Activated Human Bone Marrow Stromal Cells for Bone Repair, J. Funct. Biomater. 13 (2) (2022).

[33] K. Man, H. Joukhdar, X.D. Manz, M.Y. Brunet, L.H. Jiang, J. Rnjak-Kovacina, X. B. Yang, Bone tissue engineering using 3D silk scaffolds and human dental pulp stromal cells epigenetic reprogrammed with the selective histone deacetylase inhibitor MI192, Cell Tissue Res. 388 (3) (2022) 565–581.

[34] G. Yang, Y. Xie, S. Zhao, L. Qin, X. Wang, B. Wu, Quality Control: Internal Defects Formation Mechanism of Selective Laser Melting Based on Laser-powder-melt Pool Interaction: A Review, Chinese J. Mech. Eng.: Additive Manuf. Front. 1 (3) (2022).

[35] I.G. AmirMahyar Khorasania, Umar Shafique Awana, Alireza Ghaderi, The effect of SLM process parameters on density, hardness, tensile strength T and surface quality of Ti-6Al-4V, Addit. Manuf. 25 (2019) 176–186.

[36] C. Ni, Y. Shi, J. Liu, Influences of tilt angles on microstructure and mechanical properties of 316L stainless steel parts fabricated by selective laser melting (SLM), Mater. Res. Express 6 (8) (2019).

[37] Q.C. Liu, J. Elambasseril, S.J. Sun, M. Leary, M. Brandt, P.K. Sharp, The Effect of Manufacturing Defects on the Fatigue Behaviour of Ti-6Al-4V Specimens Fabricated Using Selective Laser Melting, Adv. Mat. Res. 891–892 (2014) 1519–1524.

[38] P.E. Markovsky, D.G. Savvakin, O.M. Ivasishin, V.I. Bondarchuk, S.V. Prikhodko, Mechanical Behavior of Titanium-Based Layered Structures Fabricated Using Blended Elemental Powder Metallurgy, J. Mater. Eng. Perform. 28 (9) (2019) 5772–5792.

[39] C. Bellini, R. Borrelli, V. Di Cocco, S. Franchitti, F. Iacoviello, L. Sorrentino, Damage analysis of Ti6Al4V lattice structures manufactured by electron beam melting process subjected to bending load, Mater. Design Processing Commun. 3 (6) (2021).

[40] A.Y. Al-Maharma, S.P. Patil, B. Markert, Effects of porosity on the mechanical properties of additively manufactured components: a critical review, Mater. Res. Express 7 (12) (2020).

[41] D. Palmeri, G. Buffa, G. Pollara, L. Fratini, Sample building orientation effect on porosity and mechanical properties in Selective Laser Melting of Ti6Al4V titanium alloy, Mater. Sci. Eng. A 830 (2022).

[42] D. Barba, C. Alabort, Y.T. Tang, M.J. Viscasillas, R.C. Reed, E. Alabort, On the size and orientation effect in additive manufactured Ti-6Al-4V, Mater. Des. 186 (2020).

[43] S. Sneddon, Y. Xu, M. Dixon, D. Rugg, P.F. Li, D.M. Mulvihill, Sensitivity of material failure to surface roughness: A study on titanium alloys Ti64 and Ti407, Mater. Des. 200 (2021).

[44] I. Holland, J. Logan, J. Shi, C. McCormick, D. Liu, W. Shu, 3D biofabrication for tubular tissue engineering, Biodes Manuf 1 (2) (2018) 89–100.

[45] S.C. Cox, P. Jamshidi, N.M. Eisenstein, M.A. Webber, H. Burton, R.J.A. Moakes, O. Addison, M. Attallah, D.E.T. Shepherd, L.M. Grover, Surface Finish has a Critical Influence on Biofilm Formation and Mammalian Cell Attachment to Additively Manufactured Prosthetics, ACS Biomater. Sci. Eng. 3 (8) (2017) 1616–1626.

[46] Y. Hou, W. Xie, L. Yu, L.C. Camacho, C. Nie, M. Zhang, R. Haag, Q. Wei, Surface Roughness Gradients Reveal Topography-Specific Mechanosensitive Responses in Human Mesenchymal Stem Cells, Small 16 (10) (2020) e1905422.

[47] S. Stewart, A. Darwood, S. Masouros, C. Higgins, A. Ramasamy, Mechanotransduction in osteogenesis, Bone Joint Res. 9 (1) (2020) 1–14.

[48] F. Distefano, S. Pasta, G. Epasto, Titanium Lattice Structures Produced via Additive Manufacturing for a Bone Scaffold: A Review, J. Funct. Biomater. 14 (3) (2023).

[49] G. Osterhoff, E.F. Morgan, S.J. Shefelbine, L. Karim, L.M. McNamara, P. Augat, Bone mechanical properties and changes with osteoporosis, Injury 47 (Suppl 2) (2016) S11–S20.

[50] N. Xue, X. Ding, R. Huang, R. Jiang, H. Huang, X. Pan, W. Min, J. Chen, J.A. Duan, P. Liu, Y. Wang, Bone Tissue Engineering in the Treatment of Bone Defects, Pharmaceuticals (Basel) 15(7) (2022).

[51] R. De Biasi, S. Murchio, E. Sbettega, S. Carmignato, V. Luchin, M. Benedetti, Efficient optimization framework for L-PBF fatigue enhanced Ti6Al4V lattice component, Mater. Des. 230 (2023).